A ailable li e a . cie cedi ec .c
ScienceDirect
Acta Materialia 56 (2008) 3824–3832
Acta MATERIALIA
www.elsevier.com/locate/actamat

# Extraction of flow properties of single-crystal silicon carbide by nanoindentation and finite-element simulation

Sanghoon Shim [a,b,*], Jae-il Jang [c], G.M. Pharr [a,b]

[a] The University of Tennessee, Department of Materials Science and Engineering, Knoxville, TN 37996, USA
[b] Oak Ridge National Laboratory, Materials Science and Technology Division, Oak Ridge, TN 37831, USA
[c] Hanyang University, Division of Materials Science and Engineering, Seoul 133-791, Republic of Korea

Received 22 February 2008; received in revised form 4 April 2008; accepted 6 April 2008
Available online 28 May 2008

**Abstract**

A method is presented for estimating the plastic flow behavior of single-crystal silicon carbide by nanoindentation experiments using a series of triangular pyramidal indenters with five different centerline-to-face angles in combination with two-dimensional axisymmetric finite-element (FE) simulations. The method is based on Tabor's concepts of characteristic strain and constraint factor, which allow indentation hardness values obtained with indenters of different angles to be related to the flow properties of the indented material. The procedure utilizes FE simulations applied in an iterative manner in order to establish the yield strength and work-hardening exponent from the experimentally measured dependence of the hardness on indenter angle. The methodology is applied to a hard, brittle ceramic material, 6H–SiC, whose flow behavior cannot be determined by conventional tension or compression testing. It is shown that the friction between the indenter and the material plays a significant role, especially for very sharp indenters.


*Keywords:* Nanoindentation; Hardness; Plastic deformation; Finite-element modeling (FEM); Single-crystal silicon carbide

## 1. Introduction

The electronics industry has been dominated by silicon since the 1950s, but this situation could soon change for high-voltage switching and high-frequency power devices. In this regard, a strong candidate to replace silicon is hexagonal silicon carbide (SiC), whose commonly used forms include 4H–SiC and 6H–SiC (i.e., four or six Si–C bilayers in the unit cell, respectively) [1]. A knowledge of this material's elastic–plastic stress–strain behavior is needed to simulate deformation behavior and failure modes of structures, as well as to facilitate more precise machining of single-crystal wafers and better design of SiC-based devices. Unfortunately, however, the brittle nature of SiC makes it very hard to obtain a stress–strain data at room temperature by conventional tension or compression testing. To overcome this difficulty, we have developed a new technique for estimating the stress–strain behavior of brittle materials using a combination of nanoindentation experiments and finite-element simulations. Here, the method is presented and applied to a 6H–SiC single-crystal.

A number of papers have explored the feasibility of extracting flow properties by nanoindentation with sharp pyramidal indenters [2–12]. Numerous difficulties and limitations have been noted, including questions about the uniqueness of the measured parameters and the range of $E/\sigma_y$ (Young's modulus to yield strength ratio) and $n$ (strain hardening exponent) over which they apply. Spherical nanoindentation, for which analytical solutions and models are well known, also has some limitations due to the imperfections in tip shape and a strong dependence of measured parameters on a precise knowledge of the tip radius [13].

In this study, results from nanoindentation experiments using a series of three-sided pyramidal indenters with dif-

* Corresponding author.
*E-mail address:* shims@ornl.gov (S. Shim).

1359-6454/$34.00 © 2008 Acta Materialia Inc. Published by Elsevier Ltd. All rights reserved.
doi:10.1016/j.actamat.2008.04.013

ferent centerline-to-face angles and finite-element simulations of the indentation process are combined to estimate the plastic flow properties. Although applied to a brittle ceramic material, the methodology should be applicable to a wide range of materials including metals, ceramics and semiconductors.

## 2. Background

Since indentation testing is relatively simple and easy to perform and requires only a very small volume of material, there have been numerous efforts to obtain stress–strain curves from indentation data [2–12]. Many of these are based on the well-known relationship between hardness, $H$, and flow stress, $\sigma_f$, originally suggested by Tabor [2]:

$$H = C_\theta \cdot \sigma_f \tag{1}$$

where the flow stress is defined at "a characteristic value of plastic strain", i.e., a "characteristic strain", and $C_\theta$ is the "constraint factor" which depends on the indenter angle, $\theta$. The original source for the constraint factor concept was provided by Prandtl [14] who applied slip line field theory to flat punch indentation and found that the constraint factor is 2.57 for the Tresca yield criterion and 2.97 for the von Mises yield criterion. We note here, however, that these values formally apply only to materials that behave as rigid-plastic, i.e., $E/\sigma_y$ is very large.

In the mid-1960s, Atkins and Tabor [3] performed indentation experiments on copper and mild steel with several diamond conical indenters having different angles and showed that the hardness does indeed depend on cone angle. This means that if one can use a series of indenters with different angles and one knows the "characteristic strain ($\varepsilon_{char}$)" for a given indenter angle, it is possible to construct the stress–strain curve by relating the hardness to the stress and the indenter angle to the characteristic strain (see Fig. 1).

Usually the value of constraint factor is thought to lie in the range 2.6–3.0 [2,3], which is appropriate for metallic materials when the deformation is fully plastic. However, under certain circumstances, there can be a significant influence of the ratio of Young's modulus to yield strength ($E/\sigma_y$) on the constraint factor, as first suggested by Johnson [5]. In particular, Johnson showed that when deformation is not fully plastic, i.e., in the elastic–plastic transition range, $C_\theta$ increases as $E/\sigma_y$ increases and decreases as the indenter angle increases according to the relation:

$$C_\theta = \frac{2}{3}\left[1 + \ln\left(\frac{E}{\sigma_y}\cdot\cot\theta\right)\right] \tag{2}$$

Similarly, Bolshakov and Pharr [15] showed by finite-element simulation that the constraint factor can be quite dependent on $E/\sigma_y$, especially for ceramic materials which have relatively low $E/\sigma_y$. This is especially important in this work as the material to be experimentally measured is a hard ceramic with a low $E/\sigma_y$.

Values for the characteristic strain ($\varepsilon_{char}$) and its dependence on indenter angle have been determined in many experimental and theoretical investigations [2–12]. In his original work, Tabor found that the characteristic strain for a four-sided-pyramidal Vickers indenter is in the range 0.08–0.10. Subsequent experimental work with Atkins [3] using a variety of conical indenters of different half included angle, $\theta$, revealed characteristic strains for metals of 0.3, 0.25, 0.17, 0.11, 0.08 and 0.04 for indenter angles of 30°, 45°, 60°, 68°, 75° and 85°, respectively. Subsequently, Johnson [5] used the expanding cavity analogy to derive the simple relationship

$$\varepsilon_{char} = 0.2 \cdot \cot\theta \tag{3}$$

which is often used to estimate the characteristic strain for materials and conditions for which plasticity is fully developed.

Motivated by the widespread application of nanoindentation in the 1990s, a number of studies have recently been conducted to further develop these ideas. Based on the equivalent plastic strain concept and finite-element calculations, Jayaraman et al. [6] suggested characteristic strains of 0.070 and 0.225 for the Berkovich and cube-corner indenters, respectively. Cheng et al. [8] performed extensive finite-element calculations and dimensionless analysis on wide range of materials, and suggested that the characteristic strain (for $45° \leqslant \theta \leqslant 80°$) can be approximated by

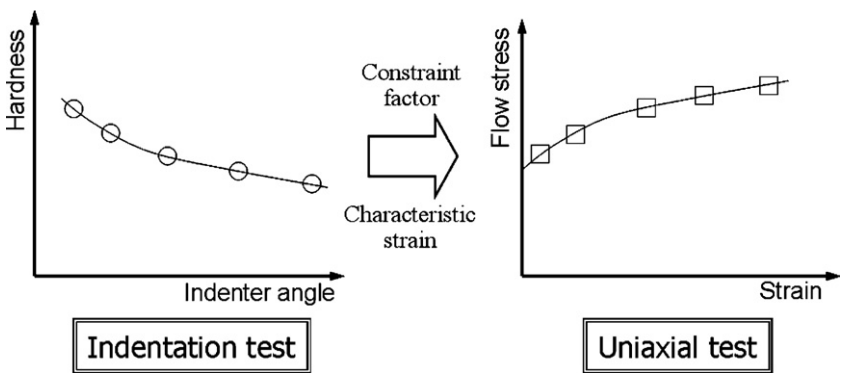


Fig. 1. Schematic diagram illustrating Tabor's concept for estimating the stress–strain curve from hardness measurements made with indenters of various angles.

$$\varepsilon_{\text{char}} = -0.0061 \cdot \theta + 0.5344 \quad (\theta \text{ in degrees}) \tag{4}$$

All of these apply mostly to metals for which $E/\sigma_y$ is relatively large. For ceramics, $E/\sigma_y$ is typically small, and the characteristic strains and constraint factors may be very different.

Using the procedure of "graphical superposition," which superimposes indentation data on the single master curve for various $E/\sigma_y$ values, Sakai et al. [12] conducted finite-element analyses for elastic–perfectly plastic and elastic–linear strain hardening conical indentations, and suggested

$$\varepsilon_{\text{char}} = 0.22 \cdot \cot\theta \tag{5}$$

which is very similar to Eq. (3). They also showed how the constraint factor depends on friction. However, they did not consider how friction affects the characteristic strain, and they considered only linear work-hardening rather than power law work-hardening. For this reason, we adapt another approach based on experimental observations combined with finite-element simulations.

Like many other studies, our approach is based on the assumption that the uniaxial elastic–plastic constitutive behavior can be described by the power law relation:

$$\sigma_f = K \cdot \varepsilon^n \tag{6}$$

where $K$ is the strength coefficient, $n$ is the work-hardening exponent and $\varepsilon$ is the uniaxial strain. As shown in Fig. 2, we assume that the behavior is elastic up to the yield strength, which then implies that $K = \sigma_y(\sigma_y/E)^{-n}$. By combining Eqs. (1) and (6) and taking the common logarithm, the hardness can be expressed as

$$\log H = n \cdot \log\left(\frac{E}{\sigma_y} \cdot \varepsilon_{\text{char}}\right) + \log(C_\theta \cdot \sigma_y) \tag{7}$$

This suggests that a plot of $\log H$ vs. $n$ should be linear with a slope related to the characteristic strain, $\varepsilon_{\text{char}}$, and an intercept related to the constraint factor $C_\theta$. In the next section, we show how $\varepsilon_{\text{char}}$ and $C_\theta$ can be determined from a limited number of finite-element calculations performed in an iterative scheme. The process converges quickly and results in an estimation of $K$ and $n$ from the measured dependence of hardness on indenter angle and a known value for $E$. Friction plays an important role, which is also explored.

## 3. Experimental and finite-element procedures

### 3.1. Experiments

A 250-μm-thick wafer of (0001) 6H–SiC single-crystal was tested using a Nanoindenter-XP (MTS Nano Instruments, Oak Ridge, TN). Five different three-sided pyramidal indenters having centerline-to-face angles, $\theta$, of 35.3° (cube-corner indenter), 45°, 55°, 65.3° (Berkovich indenter), and 75° were employed. Maximum indentation loads were varied in the range from 10 to 100 mN and loading/unloading rates were fixed at 0.5 and 5 mN s$^{-1}$. Within the range of indentation loading/unloading rates examined, no rate effects on the indentation curves were observed. After indentation tests, all the hardness impressions were imaged using a Leo 1525 field-emission scanning electron microscopy (Carl Zeiss SMT Inc., Thornwood, NY) to measure actual contact areas in a manner that accounts for pile-up around the hardness impressions.

### 3.2. Finite-element analysis (FEA)

Two-dimensional finite-element simulations of conical indentation of a semi-infinite half space were conducted using the commercial finite-element package ABAQUS (Hibbit, Karlson and Sorensen Inc., Providence, RI) [16]. Half-included angles for the conical indenters were 42.3°, 52.1°, 61.4°, 70.3° and 78.2° corresponding to centerline-to-face angles of 35.3°, 45°, 55°, 65.3° and 75°, respectively, for the three-sided pyramidal indenters used in experiment,

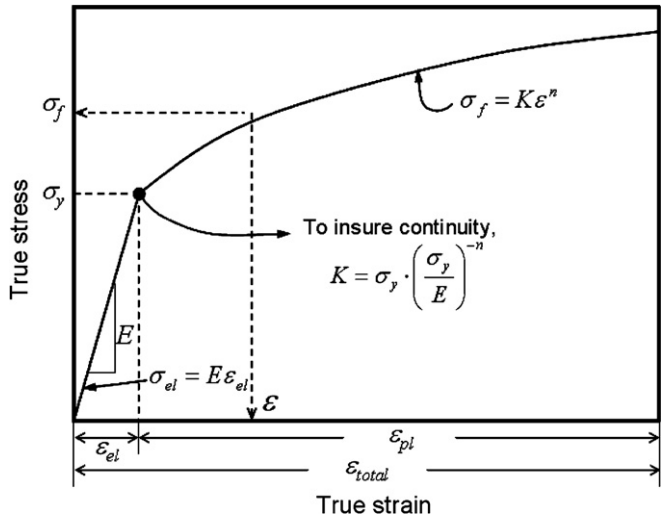


Fig. 2. True stress–true strain curve for a power law hardening material.

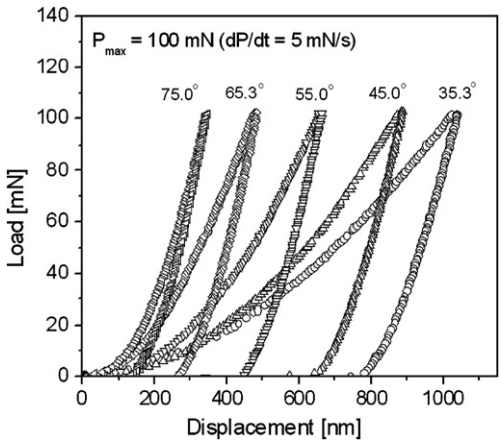


Fig. 3. Load–displacement curves for indenters with various centerline-to-face angle, $\theta$. Results are from tests at $P_{\max} = 100$ mN and $dP/dt = 5$ mN s$^{-1}$.

that is, the indenter angles were chosen to give the same area-to-depth ratios.

All calculations were carried out using an axisymmetric specimen modeled as a cylinder 200 μm in both length and radius with four-node linear axisymmetric elements. In order to measure contact areas very accurately, a very fine mesh was used near the indenter tip in the region of contact. The calculations were continued until the contact area included at least 10 elements for the sharpest indenter, and more generally 20–30 elements. A sensitivity study showed that the meshes adequately simulated the behavior of a semi-infinite solid.

Isotropic elastic constants of $E = 300$ GPa (measured from Berkovich indentation in this study) and $v = 0.24$ (generally accepted for SiC) were employed in the calculations. Power law hardening behavior was characterized by various work-hardening exponents of 0.0, 0.1, 0.2, 0.3 and 0.4. The friction coefficient between the rigid indenter and

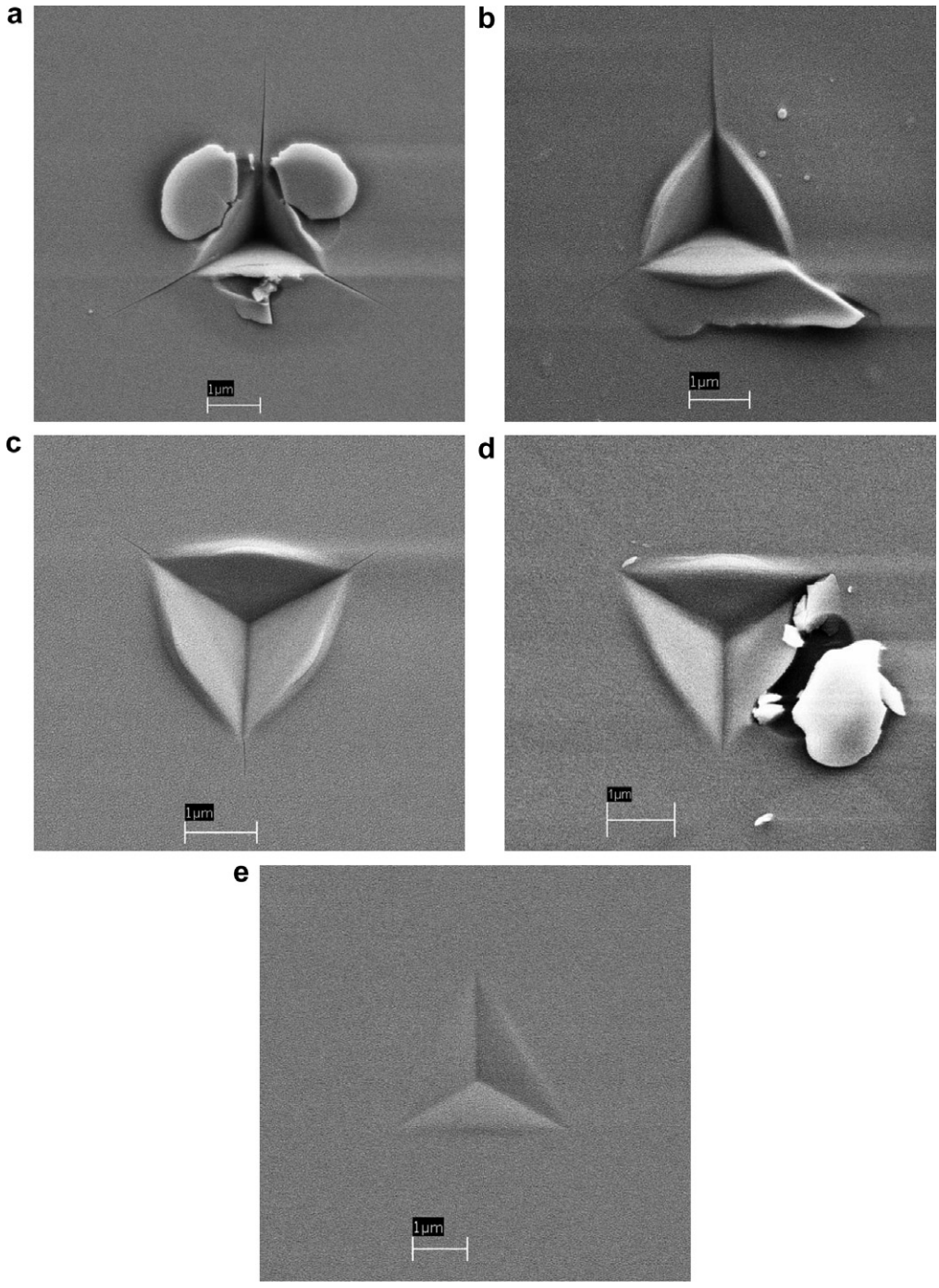


Fig. 4. SEM micrographs of indentations made with indenters of various angles at $P_{max} = 100$ mN and $dP/dt = 5$ mN s$^{-1}$: (a) 35.3° (cube-corner indenter); (b) 45.0°; (c) 55.0°; (d) 65.3° (Berkovich indenter); (e) 75.0°. Note that the magnification of each image is not the same.

the specimen was taken as 0.0 for the ideal frictionless case and 0.2 for the more realistic case. The latter value was determined from a scratch test on the same material [17].

## 4. Estimating the stress–strain curve by finite-element simulation

### 4.1. Step I – nanoindentation experiments and initial FE analysis

The first step in the process is to perform nanoindentation experiments with the five indenters having different centerline-to-face angles. Fig. 3 shows a representative example of load–displacement ($P$–$h$) curves obtained at $P_{max} = 100$ mN. As one might expect, with decreasing indenter angle, the displacement at the peak load increases and a larger portion of irreversible plastic deformation is observed. Note that the Oliver–Pharr method [18] cannot be directly applied to hardness evaluation here for two reasons. First, the constant $\beta$ that relates stiffness to contact area is a function of indenter angle and is not known well for any of the indenters except the Berkovich. Second, the Oliver–Pharr method does not account for pile-up, which is clearly evident for the sharper indenters. Therefore, we took a series of scanning electron microscopy (SEM) images to measure the size of the hardness impressions (see Fig. 4). We assume here that the cracking does not influence on the measured hardnesses. Fig. 5 summarizes the variation in hardness with indenter angle based on the SEM observations. It is seen that hardness increases with decreasing indenter angle. Note that the hardness does not significantly change with maximum indentation load, indicating that the indentation size effect [19] is not particularly strong in this material. To minimize the errors which could be introduced by measuring the size of the hardness impressions, only the hardness values obtained at the highest indentation load ($P_{max} = 100$ mN) were used in the FEM-based analysis. The values are listed in Table 1.

From the Berkovich ($\theta = 65.3°$) indentations at 100 mN, we obtained $E \cong 300$ GPa by the Oliver–Pharr method [18], and used this as Young's modulus in the calculations. To begin the simulations, we first guessed the yield strength very roughly based on the hardness values from Berkovich indentations ($H \cong 22$ GPa, see Table 1). Because SiC has a relatively low $E/\sigma_y$ ($E/\sigma_y \cong 30$–$50$), we initially assumed a constraint factor of 2.0 rather than 3.0 (the common value for metallic materials), and estimated the yield strength as 11 GPa. Finite-element calculations were then performed assuming no work-hardening but varying $\sigma_y$ (i.e., $n = 0$). The results shown in Fig. 6 show that the yield strength is close to $\sigma_y = 10$ GPa when it is assumed there is no work-hardening.

### 4.2. Step II – determination of $C_\theta$ and $\varepsilon_{char}$

The second step provides an initial estimate of the constraint factor ($C_\theta$) and characteristic strain ($\varepsilon_{char}$) based on a series of finite-element simulations. With a constant yield strength of 10 GPa (first estimate from step I) and various work-hardening exponents ($n = 0$, 0.1, 0.2, 0.3 and 0.4), indenter angles ($\theta = 42.3°$, 52.1°, 61.4°, 70.3° and 78.2°) and friction coefficients ($\mu = 0$ and 0.2), 50 sets of calculations were performed to get a hardness value for every

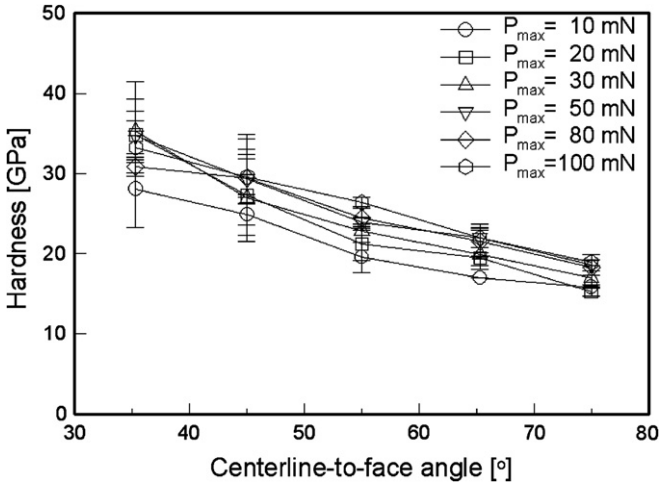


Fig. 5. Change in experimentally measured hardness with indenter angle. Error bars indicate maximum and minimum values.

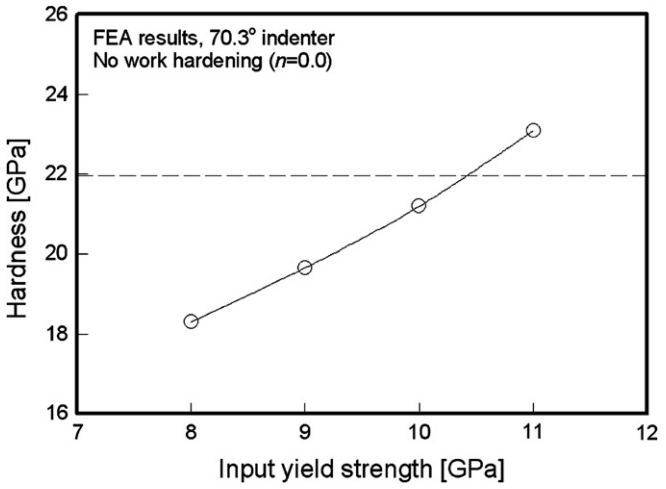


Fig. 6. FEA results for estimating the initial yield strength value ($n = 0$).

Table 1
Experimentally measured nanoindentation hardnesses of a 6H–SiC single-crystal

| Indenter angle, $\theta$ (°) | 35.3 | 45.0 | 55.0 | 65.3 | 75.0 |
|---|---|---|---|---|---|
| Hardness (GPa) | 33.27 ± 3.65 | 29.60 ± 3.42 | 26.40 ± 0.79 | 21.98 ± 1.88 | 18.91 ± 0.40 |

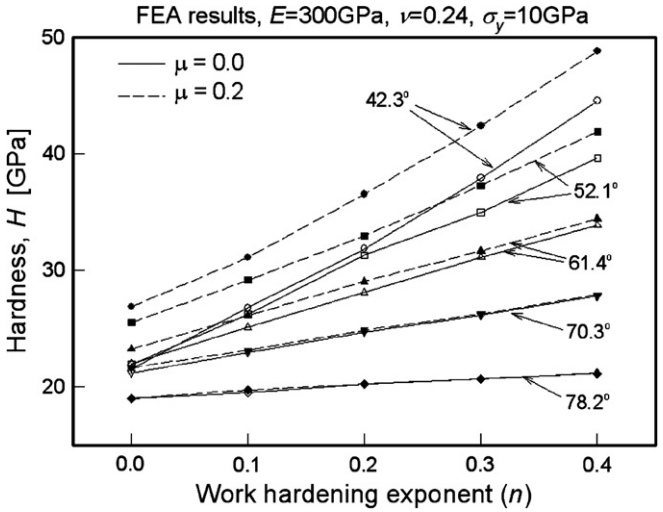


Fig. 7. Hardness dependence on indenter angle, work-hardening exponent and friction coefficient.

combination of $n$, $\theta$ and $\mu$. The calculation results are shown in Fig. 7. The hardness increases dramatically with increases in both work-hardening exponent and friction coefficient and decreases in indenter angle. The results for $n = 0$ allow us to estimate the constraint factor for each indenter angle by means of Eq. (1). The hardnesses for $n = 0$ are shown in Fig. 8, and the constraint factors derived from them are summarized in Table 2. Note that

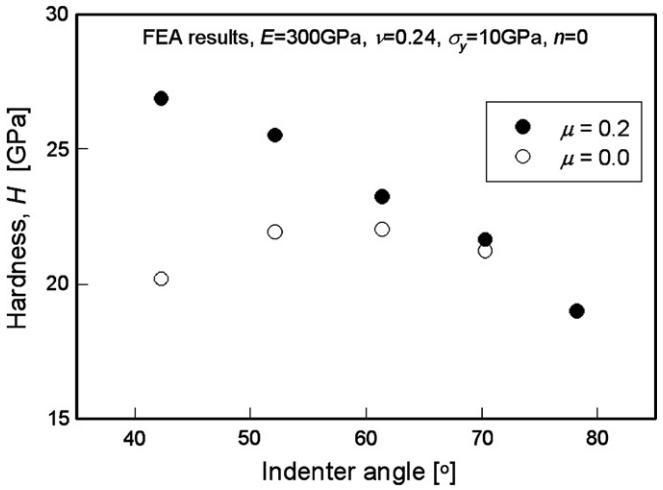


Fig. 8. FEA results to evaluate the constraint factor.

the constraint factor from finite-element analysis is 1.9–2.2 for $\mu = 0$ and 1.9–2.7 for $\mu = 0.2$ and depends on the indenter angle. Note also that the friction coefficient plays an important role, especially in determining the hardness and constraint factor for relatively sharp indenters, which is in agreement with other reports in the literature [12,20,21]. According to a simple model suggested by Bucaille et al. [11], for $\theta = 42.3°$, the normal force of indentation increases by 22% when the friction coefficient is increased from 0 to 0.2. On the other hand, friction has no significant influence on the normal force for relatively blunt indenters, i.e., indenters whose angle is greater than 60°. Based on these results, it is clear that taking friction into account is very important. One could conceivably implement this in experiments by measuring the friction coefficient in a scratch test. By applying the constraint factors calculated in this step, flow stress observed for each indenter can be initially estimated using Eq. (1).

A first estimate of the characteristic strains can be obtained by considering how the hardness in the finite-element calculations varies with the work-hardening exponent, $n$. Fig. 9 shows plots of ($\log H$) vs. work-hardening exponent ($n$) based on the finite-element data. Each data set for a specific indenter angle indeed shows linear relation consistent with Eq. (7), and thus the characteristic strain can be calculated from the slope of the data in conjunction with the known value of $E$ and the finite-element estimate of $\sigma_y = 10$ GPa. The characteristic strains determined in this way are listed in Table 2.

### 4.3. Step III – extracting the stress–strain curve

Using the $C_\theta$ and $\varepsilon_{char}$ values calculated in step II, the experimental hardnesses of 6H–SiC (see Fig. 5 and Table 1) can be converted to flow stresses and strains to construct the stress–strain curve as shown in Fig. 10. In the first iteration, the least-square fitting of this stress–strain curve gives work-hardening exponents $n = 0.30$ and 0.19 for $\mu = 0.0$ and 0.2, respectively. Note that at this stage, the yield strength is still assumed to be 10 GPa. Since these work-hardening exponents are different from the initial guess ($n = 0$, see step I), this whole procedure must be repeated and iterated until the yield strength and work-hardening exponent converge.

A second iteration of finite-element calculations were conducted using the work-hardening exponent calculated from first iteration ($n = 0.30$ and 0.19 for $\mu = 0.0$ and

Table 2
Constraint factors and characteristic strains obtained from the first iteration

| | | | | | | |
|---|---|---|---|---|---|---|
| Indenter angle (°) | Pyramid (experiment) | 35.3 | 45 | 55 | 65.3 | 75 |
| | Cone (FEA) | 42.3 | 52.1 | 61.4 | 70.3 | 78.1 |
| Constraint factor, $C_\theta$ | $\sigma_y = 10$ GPa, $\mu = 0.0$ | 2.0182 | 2.1900 | 2.2002 | 2.12 | 1.8975 |
| | $\sigma_y = 10$ GPa, $\mu = 0.2$ | 2.6850 | 2.5500 | 2.3228 | 2.1624 | 1.8989 |
| Characteristic strain, $\varepsilon_{char}$ | $\sigma_y = 10$ GPa, $\mu = 0.0$ | 0.2021 | 0.1484 | 0.0979 | 0.0651 | 0.0438 |
| | $\sigma_y = 10$ GPa, $\mu = 0.2$ | 0.1502 | 0.1151 | 0.0888 | 0.0628 | 0.0433 |

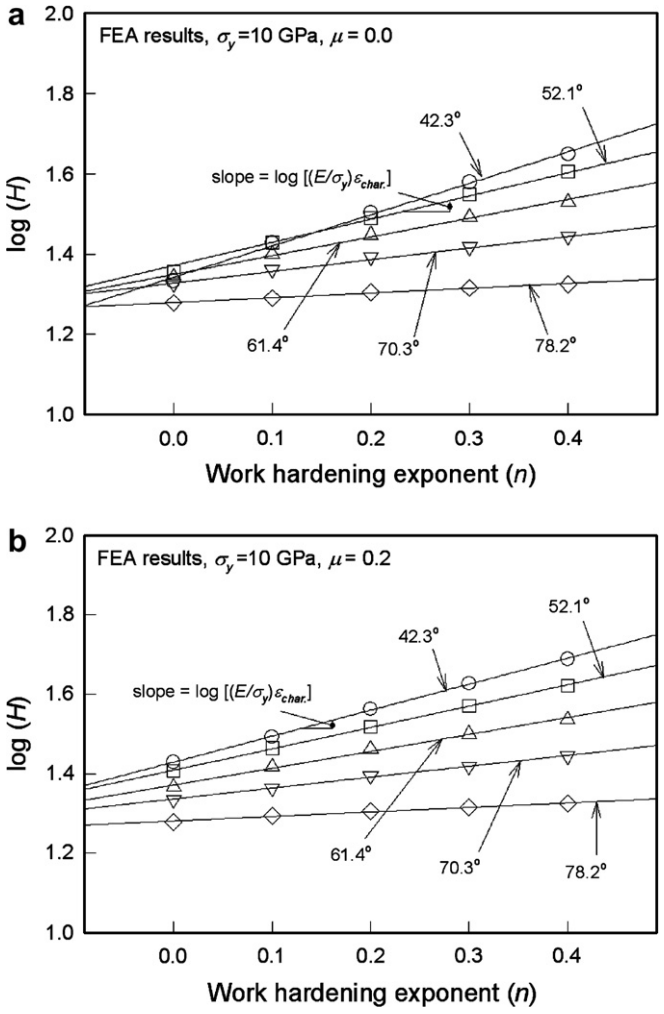


Fig. 9. FEA results to evaluate characteristic strain: (a) $\mu = 0.0$; (b) $\mu = 0.2$.

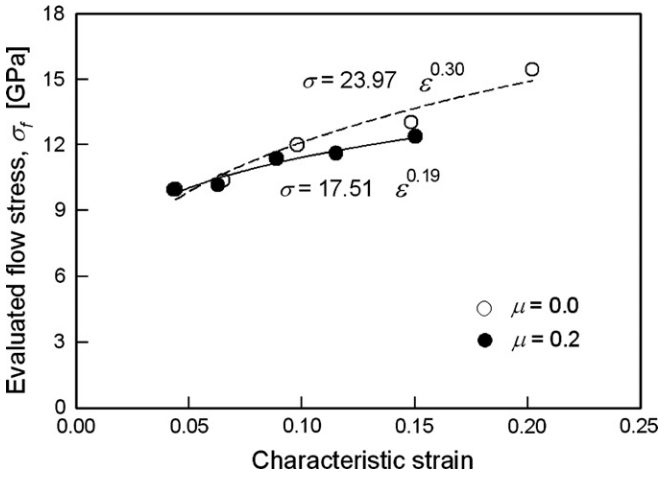


Fig. 10. Stress–strain curve estimated from nanoindentation data in conjunction with finite-element simulations in the first iteration of finite-element calculations.

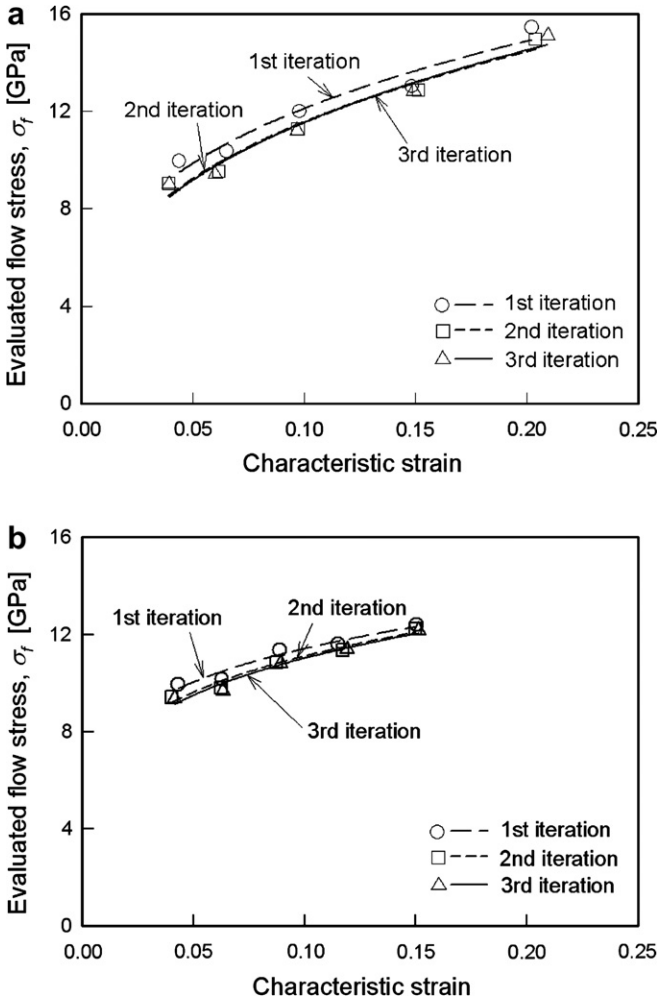


Fig. 11. Stress–strain curves estimated from nanoindentation experiments: (a) $\mu = 0.0$; (b) $\mu = 0.2$.

0.2). As a result, yield strengths of 7.2 GPa (for $\mu = 0.0$ and $n = 0.30$) and 8.5 GPa (for $\mu = 0.2$ and $n = 0.19$) were determined. These values gave a Berkovich ($\theta = 70.3°$) hardness close to 22 GPa, i.e., very close to the experimental Berkovich hardness listed in Table 1. With these second yield strength values, another set of 50 finite-element calculations were subsequently performed and new estimates for the constraint factors and characteristic strains were obtained. The process was repeated through a second and third iteration, after which reasonable convergence was achieved, as shown in Fig. 11. The flow properties of 6H–SiC determined through all of the above steps are summarized in Table 3. The dependence of the characteristic strains on indenter angle are shown and compared to results of other studies in Fig. 12. The characteristic strains determined in this study are generally lower due to the fact that the $E/\sigma_y$ for SiC is lower than that of the materials examined in the other studies, which were more metallic like. Thus, in estimating the flow properties of hard ceramic materials, it is important to consider how the characteristic strain depends on $E/\sigma_y$ as well as $\theta$ and $\mu$.

Although it is desirable to compare our results with stress–strain data from the literature, uniaxial tension or compression tests of single-crystal SiC cannot be carried

Table 3
Flow properties of 6H–SiC single-crystal wafer extracted in present study

| Results from each iteration | Friction coefficient, $\mu$ | Yield strength, $\sigma_y$ (GPa) | Work-hardening exponent, $n$ |
|---|---|---|---|
| First | 0.0 | 10.0 | 0.2958 |
| | 0.2 | 10.0 | 0.1854 |
| Second | 0.0 | 7.2 | 0.3238 |
| | 0.2 | 8.5 | 0.2065 |
| Third | 0.0 | 7.0 | 0.3297 |
| | 0.2 | 8.3 | 0.2139 |

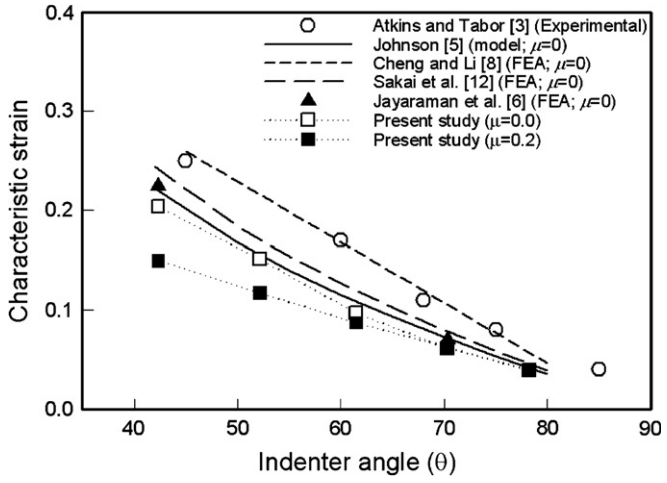


Fig. 12. Characteristic strain values suggested in previous studies.

out at room temperature without catastrophic failure of the specimen. As a result, the only data available are for elevated temperature tests [22–30], where the dislocation mobility is great enough to produce plasticity instead of fracture. Fig. 13 summarizes results for the critical resolved shear stresses ($\tau_{CRSS}$) obtained in compression tests of bulk single-crystal SiC samples at elevated temperatures and various strain rates. One could argue that the room-temperature strength can be estimated by a simple linear extrapolation of the high temperature data to room temperature. For the 4H– and 6H–SiC data in Fig. 13, this extrapolation (see extrapolation line 1 in Fig. 13) gives $\tau_{CRSS} \approx 11{,}000$ GPa. Using the same approach, extrapolation of only the 6H–SiC data excluding that above 1100 °C, which corresponds to a change in the deformation mechanism [26], gives $\tau_{CRSS} = 301$ GPa (see extrapolation line 2 in Fig. 13). Both values are clearly too high since the theoretical shear strength of the material ($\tau_{th} \approx G/10$) [31] is about 12 GPa (assuming $E = 300$ GPa and $\nu = 0.24$). A more detailed estimation of the theoretical shear strength of β-SiC based on density functional theory gives $\tau_{th} = 32$ GPa [32]. Whatever the exact value, it is clear that linear extrapolation of the high-temperature data significantly overestimates the strength and is not reliable. Moreover, based on measurements of nanoindentation pop-in of 6H–SiC, Page et al. concluded that the theoretical shear strength is about 6.8 GPa [33]. Thus, the yield strengths deduced in this work of 7.2 and 8.5 GPa (for $\mu = 0$ and 0.2, respectively) appear to be reasonable.

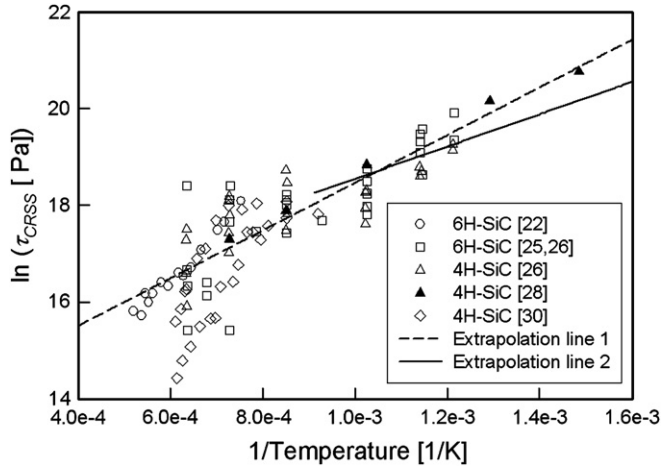


Fig. 13. Temperature dependence of the critical resolved shear stress, $\tau_{CRSS}$, for data from Refs. [22–30].

## 5. Summary and conclusions

Nanoindentation experiments utilizing various three-sided indenters with different angles and finite-element calculations were performed to evaluate the stress–strain curve of a 6H–SiC single-crystal. Results from both the experiments and finite-element simulations were combined to produce a new procedure for determining the yield strength, characteristic strain, and work-hardening exponents for a brittle material. The procedure is summarized in Fig. 14. It is noteworthy that friction coefficient has a significant effect on the converged values for very sharp indenters, and thus on the extracted stress–strain curve.

The above results show that if: (1) a power law constitutive equation holds for the tested material and (2) the fric-

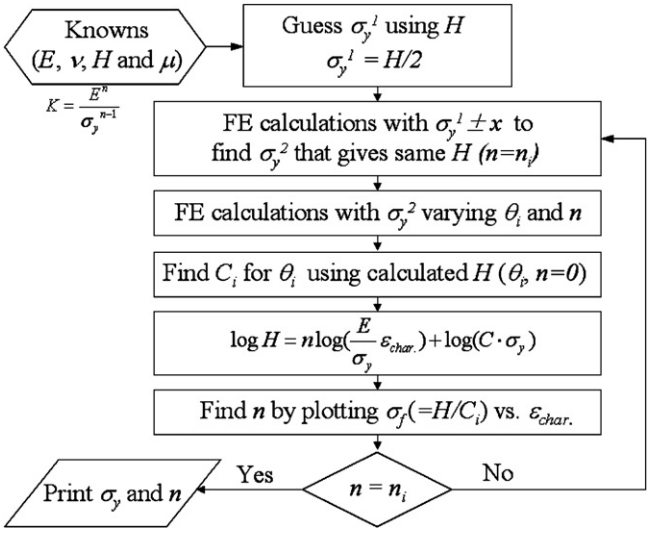


Fig. 14. Closed-loop flowchart for evaluating flow properties.

tion coefficient is known, it is possible to estimate the true stress–true strain curve of the material. However, some uncertainties and difficulties still remain. First, it is not possible to verify the procedure for SiC since its uniaxial stress–strain behavior cannot be measured at room temperature. Thus, repeating the measurements in a metallic system is desirable. Second, a significant number of finite-element calculations were needed to obtain the results. The number of calculations could be reduced considerably by conducting a large parametric finite-element study that establishes key relations needed in the analysis procedure.

## Acknowledgements

This research was sponsored by National Science Foundation under Grant No. DMR-0203552, the US Department of Energy: the Assistant Secretary for Energy Efficiency and Renewable Energy, Office of FreedomCAR and Vehicle Technologies, as part of the High Temperature Materials Laboratory User Program; the SHaRE User Facility, Division of Scientific User Facilities, and the Korea Research Foundation Grant funded by the Korean Government, MOEHRD (Grant #KRF-2006-331-D00273).

## References

[1] Zolper JC, Skowronski M. MRS Bull 2005;30:273.
[2] Tabor D. The hardness of metals. Oxford: Oxford University Press; 1951.
[3] Atkins AG, Tabor D. J Mech Phys Solids 1965;13:149.
[4] Johnson KL. J Mech Phys Solids 1970;18:115.
[5] Johnson KL. Contact mechanics. Cambridge: Cambridge University Press; 1985.
[6] Jayaraman S, Hahn GT, Oliver WC, Rubin CA, Bastias PC. Int J Solids Struct 1998;35:365.
[7] Giannakopoulos AE, Suresh S. Scripta Mater 1999;40:1191.
[8] Cheng Y-T, Li Z. J Mater Res 2000;15:2830.
[9] Dao M, Chollacoop N, Van Vliet KJ, Venkatesh TA, Suresh S. Acta Mater 2001;49:3899.
[10] Larsson P-L. Int J Mech Sci 2001;43:895.
[11] Bucaille JL, Stauss S, Felder E, Michler J. Acta Mater 2003;51:1663.
[12] Sakai M, Akatsu T, Numata S, Matsuda K. J Mater Res 2003;18:2087.
[13] Herbert EG, Oliver WC, Pharr GM. Philos Mag 2006;86:5521.
[14] Prandtl L. Nachr Ges Wiss, Gottingen. Math Phys K1 1920:74.
[15] Bolshakov A, Pharr GM. J Mater Res 1998;13:1049.
[16] ABAQUS User's Manual, version 6.4. Hibbitt, Karlson and Sorensen Inc.; 2004.
[17] Patten J. Western Michigan University; 2005, unpublished research.
[18] Oliver WC, Pharr GM. J Mater Res 1992;7:1564.
[19] Nix WD, Gao HJ. J Mech Phys Solids 1998;46:411.
[20] Mata M, Alcala J. J Mech Phys Solids 2004;52:145.
[21] Gao YF, Xu HT, Oliver WC, Pharr GM. J Mech Phys Solids 2008;56:402.
[22] Fujita S, Maeda K, Hyodo S. Philos Mag 1987;55:203.
[23] Maeda K, Suzuki K, Fujita S, Ichihara M, Hyodo S. Philos Mag 1988;57:573.
[24] Samant AV. PhD thesis, Case Western Reserve University, Cleveland, OH; 1999.
[25] Samant AV, Zhou WL, Pirouz P. Phys Status Solidi (a) 1998;166:155.
[26] Samant AV, Pirouz P. Int J Refract Met Hard Mater 1998;16:277.
[27] Samant AV, Wei XL, Pirouz P. Philos Mag 1998;78:737.
[28] Mussi A, Rabier J, Thilly L, Dement JL. Phys Status Solidi (c) 2007;4:2929.
[29] Lambrecht, Segall B. Phys Rev B 1990;41:2832.
[30] Demenet J-L, Hong MH, Pirouz P. Scripta Mater 2000;43:865.
[31] Cottrell AH. Dislocations and plastic flow in crystals. Oxford: Clarendon Press; 1953.
[32] Ogata S, Li J, Hirosaki N, Shibutani Y, Yip S. Phys Rev B 2004;70:104104.
[33] Page TF, Oliver WC, McHargue CJ. J Mater Res 1992;7:450.